Entire Process Simulation of Friction Stir Welding — Part 1: Experiments and Simulation

A combined strategy for mapping the macro- and microstructural responses of aluminum alloys was proposed

BY Y. M. XIE, X. C. MENG, AND Y. X. HUANG

Abstract

Understanding structure-parameter-property relationships in friction stir welding of aluminum alloys is a challenge despite its wide application in load-bearing components. In this paper, we propose a combined strategy for mapping the macro- and microstructural responses of these joints. A combined model based on experiment validation was adopted for the prediction of tensile strength. This included the computational fluid dynamics model, precipitation evolution model, dynamic recrystallization and recovery model, and computational solid mechanics model. The comparison between the experimental results and the combined model proved the rationality and accuracy of this numerical model.

Keywords

- Friction Stir Welding
- Aluminum Alloys
- Numerical Analysis
- Weld Process Simulation
- Mechanical Properties

Introduction

Friction stir welding (FSW), a solid-state joining technology, has become an ideal welding method to join materials with low weldability (Refs. 1, 2). The heat input, including surficial frictional and volumetric deformation heat sources, is generated by the contact between the welding tool and the workpieces, which is inversely related to the transient flow stress of the material and ensures a transient temperature just above the critical value for dynamic recovery and recrystallization (Refs. 3, 4). Several variants of FSW further enhance material flow and heat input via the structural design of the welding tools. These techniques — which can include threaded pins (Ref. 5), milling facets (Ref. 6), external scribes (Ref. 7), stationary shoulders (Ref. 1), and external heat assistance (Ref. 8) — increase the flexibility of temperature-sensitive applications. However, the more-complex deformation mechanisms have hindered the understanding of industrial applications.

As a result, new strategies to systematically analyze the entire welding process are needed. Finite element methods are acceptable underlying frameworks for a calculation strategy because they can quantitatively describe the distribution of temperature, strain, and pressure during the welding process (Ref. 9). Finite element methods can be divided into two categories: computational solid mechanics (CSM) and computational fluid dynamics (CFD) (Ref. 10). Due to the difficulty in controlling the calculation time and convergence of CSM, researchers tend to adopt the CFD method to conduct field calculation of the FSW process (Ref. 11).

Su et al. (Ref. 12) conducted an accurate prediction of thermal generation and distribution for parametric optimization. A modified constitutive equation was proposed to correct the numerical results. Arora, De, and DebRoy (Ref. 13) suggested a criterion for the design of shoulder diameters based on the principle of maximum utilization of supplied torque for traction, which established a relationship between welding tools and joint performance. Wu et al. (Ref. 14) utilized the finite element method to simulate a temperature field throughout the joint and provide a microstructural explanation. A dynamic recrystallization (DRX) analysis was conducted based on the numerical model. Using the CFD method as the underlying framework for the combined strategy, relevant field data (e.g., temperature and strain rate) could be provided based on various welding tools and parameters.

https://doi.org/10.29391/2022.101.011

A microstructural evolution containing precipitation and recrystallization behavior can further the accuracy of calculations for mechanical properties. The microstructural model inherits the outputs from the CFD model as its input. For Al-Cu-Li alloys, the precipitate model tracks three kinds of primary strengthening precipitates. dos Santos et al. (Ref. 15) calculated the fraction and radius revolution of precipitates in friction stir welded Al-Zn-Mg-Cu alloys via the Kampmann-Wagner numerical (KWN) model, proving that it is applicable for the FSW process. The DRX model is also needed. Irani, Lim, and Joun (Ref. 16) examined the application of the Johnson-Mehl-Avrami-Kolmogorov model combined with the finite element method in DRX and recovery. The accuracy between measured and predicted grain sizes was convincing. Combining the two micro models allowed the local and global mechanical properties to be subsequently calculated based on precipitation, grain boundary, dislocation, and solution strengthening (Ref. 17).

In this work, we proposed an entire process-simulation strategy based on numerical simulation to predict the tensile strength of friction stir welded joints. Third-generation aluminum alloys (AA2195-T8), which are the preferred material of rocket fuel tanks in aerospace, were chosen as the research object owing to their more-complex phase composition and precipitations. This combined model provided an accurate strategy for mapping the macro- and microstructural responses and offered sufficient datasets for the neural network methods discussed in Part 2 of this paper (Ref. 18).

Materials and Methods

The chosen object was an AA2195-T8 alloy with dimensions of 300 × 100 × 6 mm. FSW was performed at a rotational velocity of 600–1500 rpm and a welding speed of 100–500 mm/min. A plunge depth of 0.1 mm and a tilt angle of 1 deg were kept constant. A welding tool was used made of H13 steel and composed of two parts: a shoulder and a rotational pin. The rotating and stationary shoulder diameters were 14 and 18 mm, respectively. The pin size was 8 and 5.9 mm, respectively, in diameter and length, and the pin was characterized by threads and triple milling facets. The thermal cycle was recorded by several thermocouples fixed in the prefabricated blind holes that had a diameter of 1 mm.

An optical microscope (OM), KEYENCE VHX-7000, was used to observe metallography morphologies in joint transverse sections. A scanning electron microscope (Zeiss SUPRA 55) at a working voltage of 20 kV was utilized to perform an electron backscattered diffraction (EBSD) characterization with an HKL detector. The specimens for the OM and EBSD were polished by mechanical polishing and a JEOL IB-09020CP cross-section polisher, respectively. The OM specimens were etched by Keller's reagent (2.5 mL HNO_3, 1.5 mL HCl, 1 mL hydrofluoric acid, and 95 mL H_2O). An Instron® 5569 tester was applied to evaluate the tensile properties of the joints at a constant crosshead speed of 2 mm/min. The tensile samples had dimensions of 100 × 25 × 6 mm. The microhardness required for the local strength conversion was obtained by the micro Vickers hardness test with a load of 200 g and a dwelling time of 10 s.

Calculation

CFD Model

Figure 1 illustrates the schematic outline of the combined calculation strategy. As the underlying framework, the CFD model served as a converter from primitive causative variables to field variables, including strain rate and temperature. The materials to be welded and simulated, AA2195-T8 alloys, were treated as incompressible, non-Newtonian fluid. In accordance with the Boussinesq approximation, the change of alloy density was ignored during the simulation process. The tilt angle and plunge depth were taken in the same way as the experimental settings. The calculation was chosen as the steady mode to obtain the quasi-steady state of the welding process. The domain for calculation with coordinates of 60 × 90 × 6 mm was used.

The materials in the domain were described as an incompressible fluid with a constant density (Ref. 19). The deformation and flow behaviors followed the Navier-Stokes equations and the Boussinesq approximation (Ref. 20), which were solved using the finite volume method via the Fluent software:

$$\nabla \cdot v = 0 \tag{1}$$

$$\rho \frac{dv}{dt} = -\nabla P + \nabla \cdot \sigma \tag{2}$$

$$\rho c_p \frac{dT}{dt} = -\nabla(k\nabla T) + (\sigma : \nabla v) - \phi \tag{3}$$

where ρ is the density of the AA2195-T8 alloy, t is the step time, v is the transient velocity, $\sigma = \mu(\nabla v + \nabla v^t)$ is the deviatoric stress tensor, μ is the non-Newtonian viscosity, P is the structural pressure, T is the absolute temperature, ϕ is the source term that represents the heat generation of volumetric deformation heat and surficial frictional heat as well as the heat loss of convection and radiation, C_p is the specific heat capacity, and k is the thermal conductivity.

Because the Al-Cu-Li alloy is not fluid, the relationship between flow stress and viscosity was essential to access the real-time non-Newtonian viscosity. The equation between viscosity, equivalent strain rate, and flow stress was defined by the Perzyna viscoplasticity model (Ref. 21):

$$\mu = \frac{\sigma_e}{3\dot{\varepsilon}_e} \tag{4}$$

where σ_e is the flow stress or yield stress, which can be defined by a constitutive equation of aluminum alloys, and $\dot{\varepsilon}_e$ is the equivalent strain rate:

$$\sigma_e = \sqrt{\frac{3}{2}\sigma_{ij}\sigma_{ij}} \quad i,j = 1,2,3 \tag{5}$$

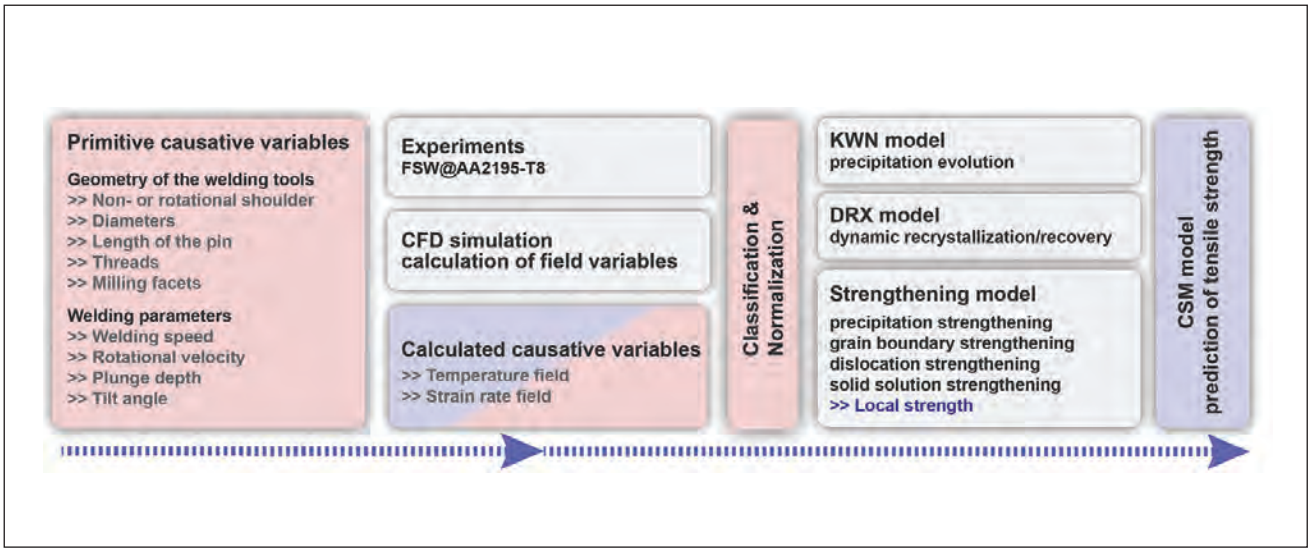

Fig. 1 — Schematic outline of the combined strategy.

$$\dot{\varepsilon_e} = \sqrt{\frac{2}{3}\dot{\varepsilon_{ij}}\dot{\varepsilon_{ij}}} \quad i,j = 1,2,3 \tag{6}$$

Here, σ_{ij} and $\dot{\varepsilon}_{ij}$ are the components of the second-order deviatoric stress tensor and the second-order strain rate tensor, respectively. The strain rate tensor can be defined by the Helmholtz velocity decomposition theorem:

$$\dot{\varepsilon_{ij}} = \frac{1}{2}\left(v_{i,j} + v_{j,i}\right) \quad i,j = 1,2,3 \tag{7}$$

The flow stress can be calculated by Sellars-Tegart constitutive equations based on strain rate and temperature (Ref. 22):

$$\sigma_e = \frac{1}{\alpha}\sinh^{-1}\left[\left(\frac{Z}{A}\right)^{\frac{1}{n}}\right] \tag{8}$$

Here, α, A, and n are material constants. Z is the Zener-Hollomon parameter, which is defined as follows (Ref. 23):

$$Z = \dot{\varepsilon_e} e^{\frac{Q_{zh}}{RT}} \tag{9}$$

where Q_{zh} is the activation energy and R is the gas constant.

However, there are limitations and drawbacks to Equation 8 when the temperature rises near the melting point (Ref. 12). Thus, the following modified constitutive equation was proposed:

$$\sigma_e = \left[1 - \left(\frac{T}{T_s}\right)^{\gamma}\right]\frac{1}{\alpha}\sinh^{-1}\left[\left(\frac{Z}{A}\right)^{\frac{1}{n}}\right] \tag{10}$$

where T_s is the solidus temperature of the AA2195-T8 alloy, and γ is the influencing factor.

For the heat boundary conditions, there are two parts of the heat source: frictional heat and deformation heat. Frictional heat is a surficial heat source applied to the interface between the welding tool and workpiece, which is described as follows:

$$F = \beta_1 R\omega \cdot \left[\frac{\delta\sigma_e}{\sqrt{3}} + (1-\delta)\mu P sin\xi\right] \cdot cos\theta \tag{11}$$

The deformation heat is a volumetric heat source, which can be defined as follows:

$$\Phi = \beta_2\mu\left[\begin{array}{c} 2\left(\frac{\partial u}{\partial x}\right)^2 + 2\left(\frac{\partial v}{\partial y}\right)^2 + 2\left(\frac{\partial w}{\partial z}\right)^2 \\ +\left(\frac{\partial u}{\partial y} + \frac{\partial v}{\partial x}\right)^2 + \left(\frac{\partial u}{\partial z} + \frac{\partial w}{\partial x}\right)^2 + \left(\frac{\partial w}{\partial y} + \frac{\partial v}{\partial w}\right)^2 \end{array}\right] \tag{12}$$

where β_1 and β_2 are the empirical coefficients, μ is the frictional coefficient, R is the radius of elements to the axis, ω is the rotational velocity, δ is the slip rate, P is the axial pressure, and ξ and θ represent the orientation of the element. The slip rate can be defined as follows (Ref. 24):

$$\delta = 1 - e^{-\frac{\omega R}{\delta_0 \omega_0 R_p}} \tag{13}$$

where δ_0 is an interfacial constant, ω_0 is a constant for nondimensionalization, and R_p is the radius of the pin. Additionally, in consideration of the heat dissipation by the welding tool, the interfacial thermal efficiency was defined by the following:

$$\lambda = \frac{J_D}{J_D + J_T} \tag{14}$$

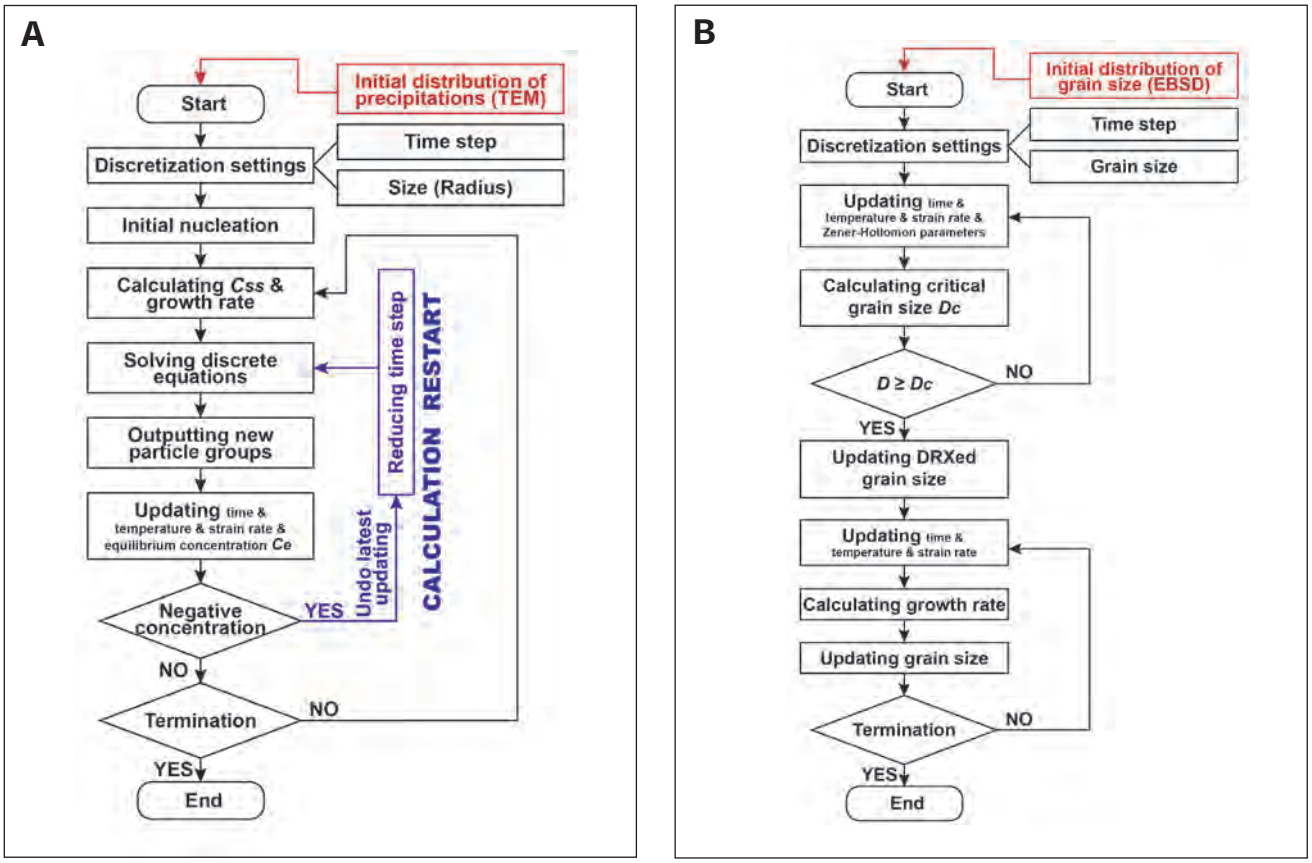

Fig. 2 — Flow charts: A — Modified KWN model; B — geometric DRX (GDRX) model.

$$J = \sqrt{k\rho C_p} \tag{15}$$

where J_D and J_T represent the domain and tool, respectively. k, ρ, and C_p are the thermal conductivity, density, and heat capacity, respectively.

The boundary heat convection and radiation can be given as follows (Ref. 25):

$$-k\frac{\partial T}{\partial z} = h(T - T_\infty) + \sigma\varepsilon(T^4 - T_\infty^4) \tag{16}$$

where h is the heat transfer coefficient, σ is the Stefan-Boltzmann constant, and ε is the emissivity of the domain.

For the motion boundary conditions, the thermo-plasticized AA2195-T8 alloy, which is regarded as a non-Newtonian fluid, was driven by the following velocity equation (Ref. 10):

$$\begin{cases} v_{horizon} = \eta\omega R \\ v_{shear} = v_{horizon} cos\xi cos\theta \\ v_{normal} = v_{horizon} cos\xi sin\theta \\ v_{vertical} = v_{horizon} sin\xi \end{cases} \tag{17}$$

The particle tracing technique was applied to assess defect formation during the FSW process. The injections were set to be massless with a random generating position of 0.3 mm in amplitude. This detailed approach refers to the work conducted by Huang et al. (Ref. 10). The distribution of particles was obtained at the section of the outlet. Areas without particles were marked as crimson (#DC143C), while the area with particles was marked as gray (#808080). The gray areas implied that the joint was sound and free of defects. An index to evaluate the distribution of these particles was expressed as:

$$\chi = \frac{\mu_R + \mu_G + \mu_B - 240}{54} \tag{18}$$

where $\mu_{R,G,B}$ are the average values of the colored section in the decimal system. The higher the index, the better the joint formation.

Microstructural Evolution Models

Precipitation evolution model. Microstructural evolution models were the secondary framework of the combined strategy. The input data for these models were taken from the CFD simulation results, which were called calculated causative variables in Fig. 1. The first part of the microstructural evolution model was the KWN precipitation evolution model. This evolution algorithm was based on the discretization of

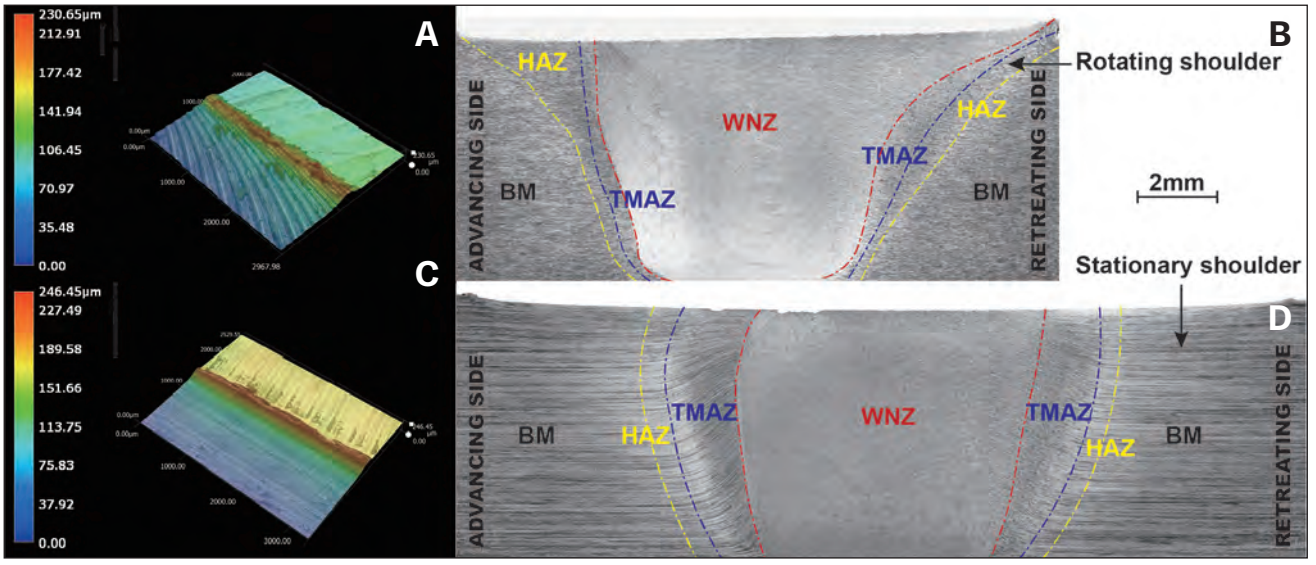

Fig. 3 — A, B — Surficial morphologies and macrostructures of the rotating shoulder with 800-rpm rotational velocity, 300-mm/min welding speed, 0.1-mm plunge depth, and 1-deg tilt angle; C, D — stationary shoulder with 1500-rpm rotational velocity, 150-mm/min welding speed, 0.1-mm plunge depth, and 1-deg tilt angle.

time and particle size. The overall calculation process mainly included three parts, as shown in Fig. 2A: (a) calculating the growth rate of precipitation particles, including dissolving and coarsening; (b) calculating the nucleation rate of particles with different sizes at each time step; and (c) recording the continuum equation of each element between the matrix and the precipitations.

Because δ' was not the major precipitation for alloys whose element ratio of Cu to Li was larger than 2.5, there were two kinds of major strengthening particles in AA2195 alloys (Ref. 26). Cu and Li elements, which constitute the T_1 and θ''/θ' phases, were the binary diffusion controlling elements. Both elements were involved in the calculation, and the element with the lower diffusion rate at the specific time prevailed. Additionally, the shapes of the two major phases were platelets rather than globular. Tremendous increases in the complexity and calculation time of the modified KWN model occurred if the influence of the phase morphology was considered.

Therefore, for the convenience of calculation, all the particles that precipitated during the welding process were treated as globular. Assuming that the ratio of radius to the thickness of the precipitations was the specific value k_s, the equivalent radius was extracted. As shown below, there was a relationship between thickness and the equivalent radius of the platelet-like precipitations.

$$r = \sqrt[3]{\frac{3k_s^2\delta^3}{4}} \tag{19}$$

where r is the equivalent radius and δ is the thickness.

The first part of the calculation process was to calculate the growth rate of the precipitation particles, which depends on the solute concentration at the interface between the particles with a certain radius and the matrix. The growth rate can be described as the following (Ref. 27):

$$v_i = \frac{\partial r_i}{\partial t} = \frac{C_{ss} - C_{int}}{C_p - C_{int}} \frac{D_f}{r_i} \tag{20}$$

where C_{ss} is the solute concentration of the diffusion-controlled element far away from the adjacent area of precipitations; C_{int} is the concentration at the interface between the precipitations and matrix, which can be calculated using the Gibbs-Thomson equation (Ref. 28); and C_p is the concentration of the diffusion-controlled element in the precipitations. When $C_{ss} < C_{int}$, the radius of particles was gradually reduced, showing the state of continuous dissolution. When $C_{ss} < C_{int}$, the radius of particles increased gradually, conversely showing the state of continuous coarsening.

D_f is the diffusion coefficient and r_i is the radius of the particle groups. Due to the severe plastic deformation essence during FSW, the dislocation density increased in an order of magnitude during the welding process, contributing to the presence of pipe diffusion (Ref. 29). This phenomenon greatly improved the diffusion rate. To reflect this characteristic in the modified KWN model, an additional coefficient was introduced into the diffusion equation, which can be written as follows (Ref. 30):

$$D_f = D_0\sqrt{1+\dot{\varepsilon}}exp\left(-\frac{Q_d}{RT}\right) \tag{21}$$

where D_0 is the diffusion factor and Q_d is the diffusion activation energy. The interfacial concentration is given by the following equation (Ref. 31):

$$C_{int} = C_e exp\left(\frac{2\gamma_{int}V_m}{r_i RT}\right) \tag{22}$$

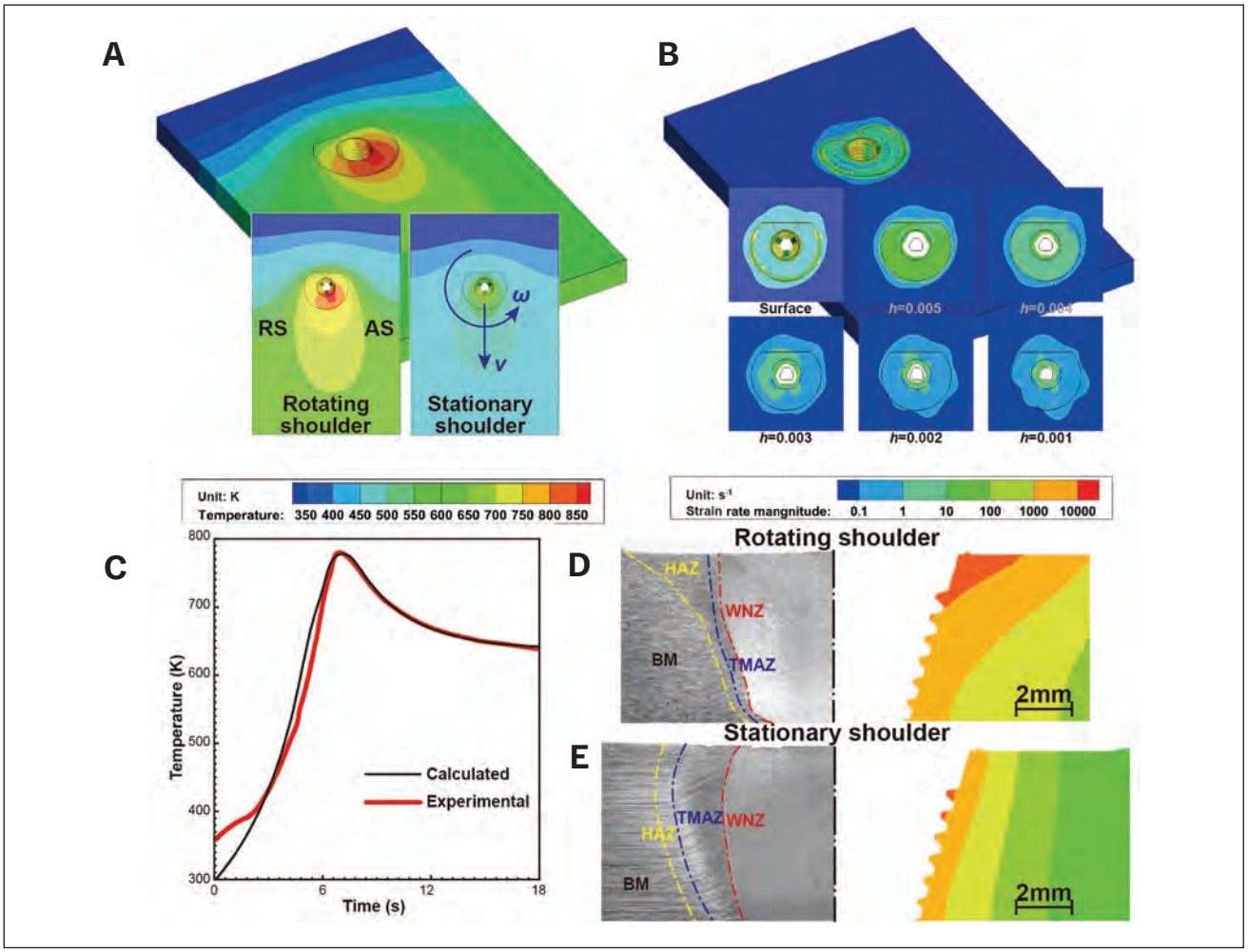

Fig. 4 — Field outputs from the CFD models: A — Distribution of quasi-steady temperature; B — distribution of quasi-steady strain rate; C — comparison of thermocouple-measured curves and numerical results. Comparisons between the calculated cross sections of friction stir welded AA2195-T8 alloy with typical welding parameters: D — rotating shoulder with rotating shoulder; E — stationary shoulder.

where C_e is the equilibrium concentration of the solute element at the interface of the matrix and precipitation; γ_{int} is the interfacial energy per unit area of the particles and matrix, which is influenced by the strain rate during the welding process; and V_m is the molar volume of the precipitations. The equilibrium concentration C_e can be calculated using the following equation:

$$C_e = C_{e0} exp\left(-\frac{Q_e}{RT}\right) \quad (23)$$

where C_{e0} is a constant and Q_e is the dissolution enthalpy of the precipitations. According to Equations 20–23, the critical radius between coarsening and dissolution can be given if $C_{ss} = C_{int}$:

$$r^* = 2\gamma_{int} V_m \left[RT \prod_{i=1}^{n} ln\left(\frac{C_{iss}}{C_{ie0}}\right) + Q_e\right]^{-1} \quad (24)$$

The second part of the calculation process was to calculate the nucleation rate at each time step. Ignoring the incubation time required to generate nuclei for precipitations, the nucleation rate can be expressed based on the effect of strain rate (Ref. 9):

$$J_{nucl} = \frac{J_0\sqrt{1+\dot{\varepsilon}}}{\sqrt{T}} exp\left\{-\frac{A_0}{(RT)^3[ln(C_{ss}/C_e)]^2} - \frac{Q_d}{RT}\right\} \quad (25)$$

$$J_0 = \frac{2\rho_{dis} V_a D_0 C_{at}\sqrt{\gamma_{int}}}{a^4 b\sqrt{k}} \quad (26)$$

$$A_0 = \frac{16\pi\varphi_i {\gamma_{int}}^3 N_A {V_m}^2}{3{C_p}^2} \quad (27)$$

where ρ_{dis} is the dislocation density that provides the position for nucleation, V_a is the volume of the matrix atom, k is the Boltzmann constant, C_{at} is the atom fraction of the

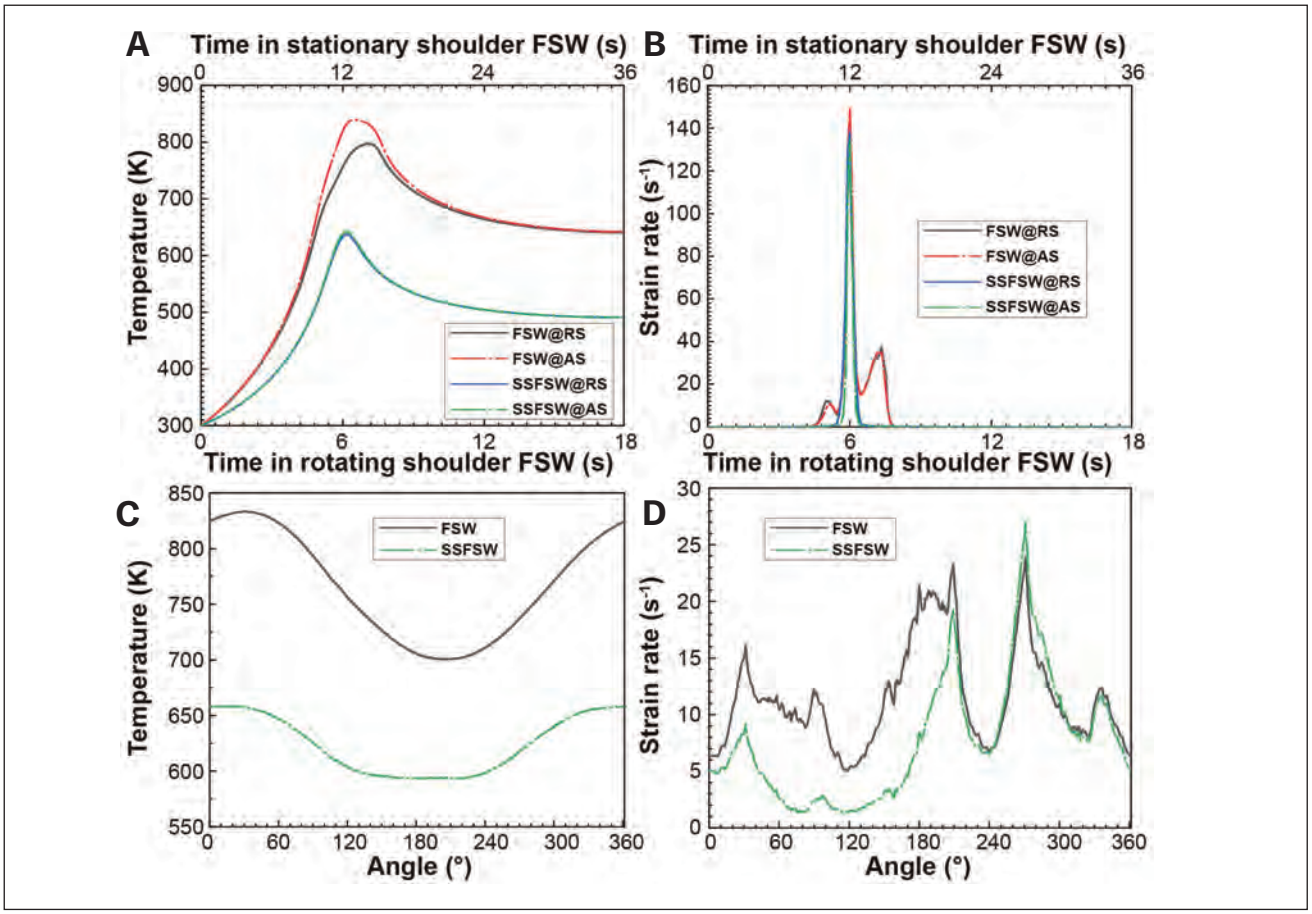

Fig. 5 — Simulated curves of temperature (A) and strain rate (B) along the streamline. Simulated curves of temperature (C) and strain rate (D) around the welding tool. Note: SSFSW refers to the FSW stationary shoulder, AS refers to the advancing side, and RS refers to the retreating side.

diffusion-controlled element in the matrix, a is the lattice constant of the matrix, b is the Burgers vector, φ_i is the wetting constant at dislocation, and N_A is Avogadro's number.

The last part of the calculation process was recording the continuum equation. The core of the particle grouping strategy was to discretize particles according to radii, simultaneously simulating nucleation, dissolution, and coarsening. Various groups of particles with different numbers flowed between the given control equation. Two kinds of precipitates were divided from small to large into groups with a fixed radius. Each particle group can be defined as a control body and can be an instance of the group class. Therefore, the nucleation, dissolution, and coarsening of particles can be written as methods of the group class, which symbolizes the source term, inflow, and outflow of the group instance. The material flow equation based on the material flow can be written as follows:

$$\frac{\partial N}{\partial t} = -\frac{\partial F_n}{\partial r} + \phi_n \tag{28}$$

where N is the number density of the particles in each particle group; F_n is the material flow; and ϕ_n is the source term, which refers to the nucleation rate at each time step. The material flow is described based on the equation of growth rate:

$$F_n = \Delta N v \tag{29}$$

Therefore, the first-order upwind material flow equation is further expressed as follows:

$$\frac{\partial N_i}{\partial t} = \begin{cases} \dfrac{\partial F_{n,i-1}}{\partial r_{i-1}} - \dfrac{\partial F_{n,i+1}}{\partial r_{i+1}} + \phi_{n,i} & F_{n,i-1} > 0, F_{n,i+1} < 0 \\ -\dfrac{\partial F_{n,i+1}}{\partial r_{i+1}} + \phi_{n,i} & F_{n,i-1} \le 0, F_{n,i+1} < 0 \\ \dfrac{\partial F_{n,i-1}}{\partial r_{i-1}} + \phi_{n,i} & F_{n,i-1} > 0, F_{n,i+1} \ge 0 \\ \phi_{n,i} & F_{n,i-1} \le 0, F_{n,i+1} \ge 0 \end{cases} \tag{30}$$

The explicit continuum equation among all the particle groups and the matrix can be given as follows:

$$C_{ss} = \frac{C_0 - C_p \sum f_v^{\,i}}{1 - \sum f_v^{\,i}} \tag{31}$$

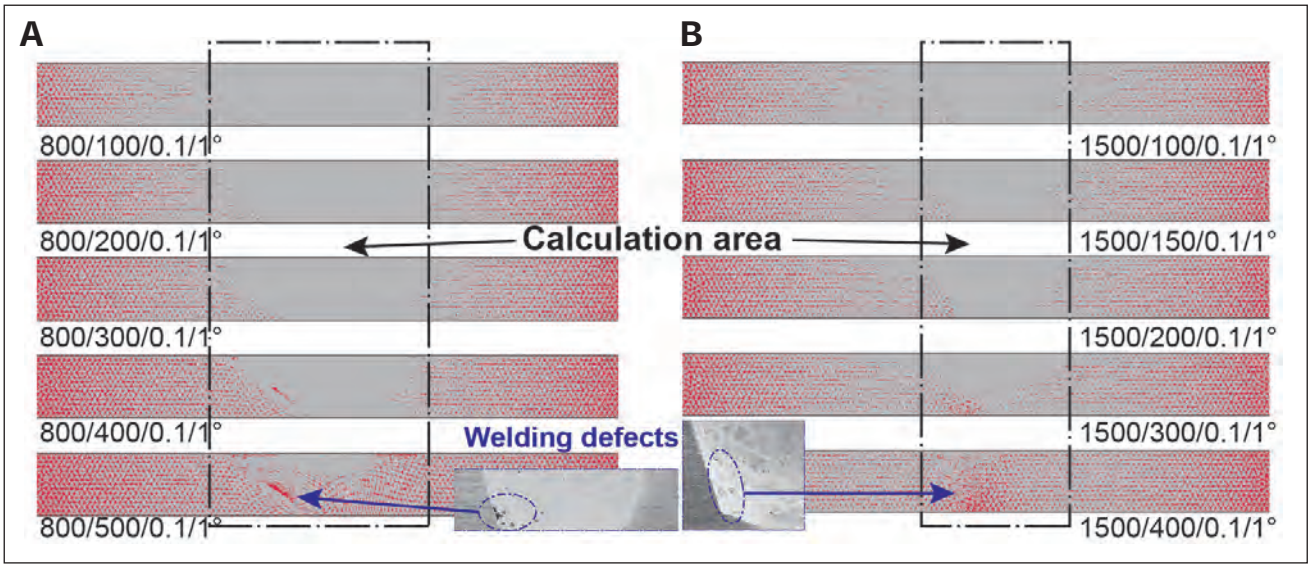

Fig. 6 — Predictions of welding parameters via the massless discrete phase model: A — Rotating shoulder; B — stationary shoulder. The labels under each figure refer to rotational velocity, welding speed, plunge depth, and tilt angle.

$$f_v^{\ i} = \frac{4}{3}\pi r_i^3 N_i \tag{32}$$

where C_0 is the total concentration of the diffusion-controlled element; f_v^i is the volume fraction of each particle group based on the globular assumption; and $\sum f_v^i$ is the volume fraction of the precipitation, which the particles pointed to. An accuracy issue existed in the calculation because the matrix concentration was obtained by updating the previous time step. The value of the time step needed to be focused on to avoid negative concentration. In other words, the change between two adjacent time steps should not be too large. An adaptive step time was applied using an auto-restart strategy — Fig. 2A.

Dynamic recrystallization model. The existing research usually indicate that DRX is mainly dominated by geometric DRX (GDRX) (Ref. 32). Therefore, the DRX behaviors in the joint — including the welding nugget zone (WNZ), thermo-mechanically affected zone (TMAZ), and heat-affected zone (HAZ) — were calculated based on GDRX mechanisms. The critical grain size of GDRX can be calculated with the following equation:

$$D_C = (a + b\ln Z)^{-1} \tag{33}$$

where a and b are the constants, and Z is the Zener-Hollomon parameter mentioned in Equation 9. The criteria can be used to determine whether GDRX occurred (no recrystallization occurred when the current grain size was greater than D_C). This is what happened to the HAZ. Recrystallization occurred when the current grain size was smaller than or equal to D_C. The initial dynamic recrystallized (DRXed) grain size was equal to D_C. For the subsequent calculation of grain size evolution, the following assumptions were made: (a) DRX occurred instantaneously when the critical recrystallization size was reached; (b) the dynamic recrystallized (DRXed) grains only underwent coarsening with subsequent deformation; (c) in the subsequent thermal process, the grains grew statically with the formation of high-angle grain boundaries. Additionally, there were precipitations in Al-Cu-Li alloys; the pinning effect of these particles should be considered (Ref. 33). The growth equation of grains is expressed as follows:

$$\frac{dD}{dt} = M_0\left(\frac{2\gamma_b}{D} - \sum\frac{3\gamma_b \sum f_v^{\ i}}{2r}\right) exp\left(-\frac{Q_G}{RT} - \dot{\varepsilon}\right) \tag{34}$$

where M_0 is the migration coefficient of grain boundaries, γ_b is the grain boundary energy, D is the diameter of grains, $\sum f_v^i$ is the volume fraction of each precipitation, $\sum((3\gamma_b \sum f_v^i)/(2r))$ is the pinning effect of the major precipitations, and Q_G is the migration activation energy of the grain boundaries. One should note that this model adopted the discretization method of grain diameter, which is similar to the modified KWN model. This detailed calculating process is depicted in Fig. 2B.

Strengthening model. As a precipitation strengthening alloy, the Al-Cu-Li alloy has four major strengthening mechanisms: grain boundary strengthening, solid solution strengthening, precipitation strengthening, and dislocation strengthening. The total yield strength (the yield strength was used as the output value in this research) can be calculated by the linear addition of inherent strength and these four strengthening mechanisms (Ref. 34):

$$\sigma_{total} = \chi^p\left[\sigma_{in} + \sigma_{gb} + M(\tau_{ss} + \tau_{prec} + \tau_{dis})\right] \tag{35}$$

where χ^p is the sensitivity coefficient of defects in the joints, σ_{in} is the intrinsic strength of the aluminum alloys,

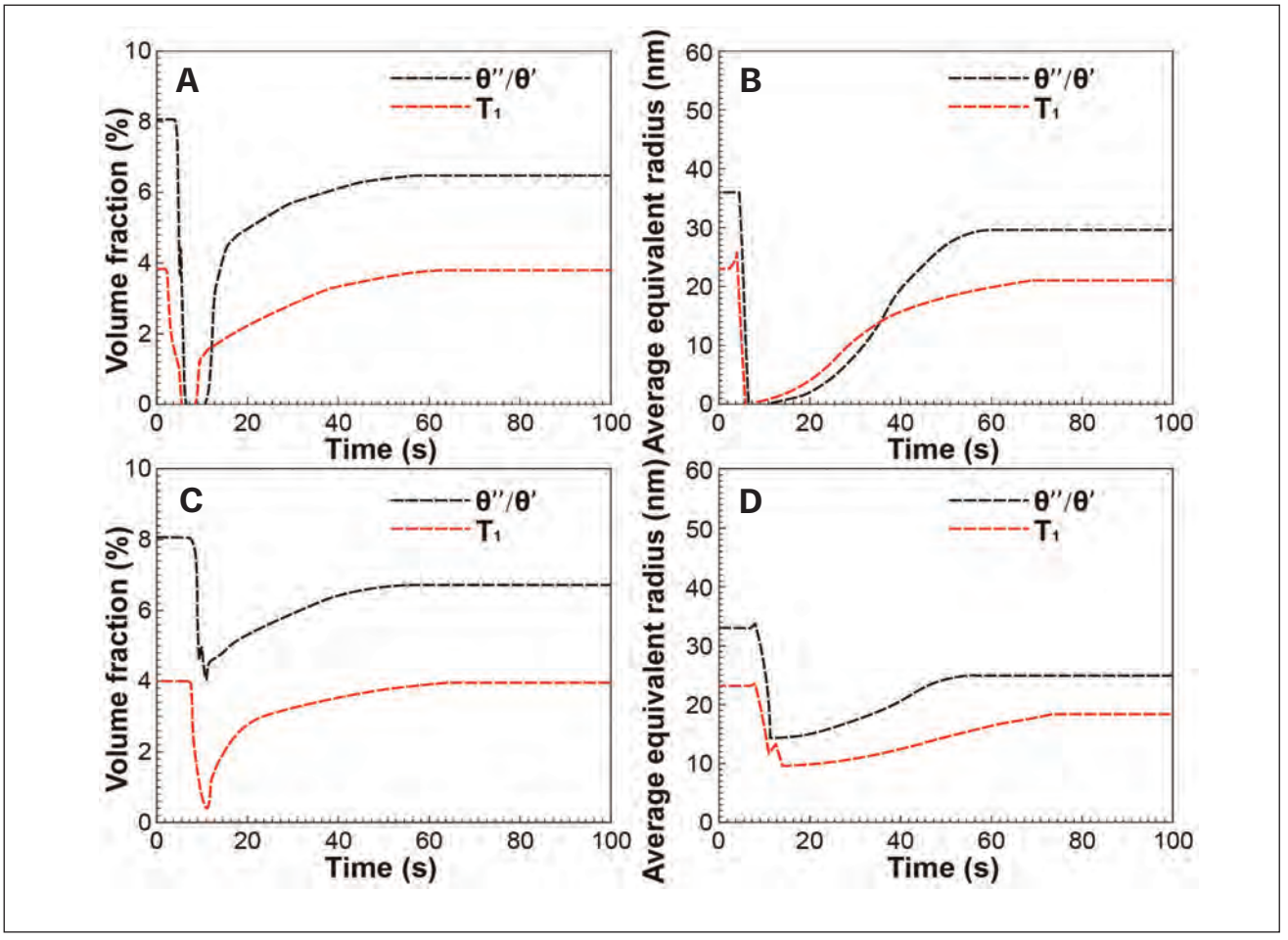

Fig. 7 — Variations of precipitations during FSW: average radius and volume fraction from the modified KWN model of the rotating shoulder (A, B) and the stationary shoulder (C, D).

σ_{gb} is the strength of the grain boundary strengthening, M is the Taylor factor (Ref. 35), τ_{ss} is the strength of the solid-solution strengthening, τ_{prec} is the strength of the precipitation strengthening, and τ_{dis} is the strength of the dislocation strengthening. The grain boundary strengthening follows the Hall-Petch formula (Ref. 36):

$$\sigma_{gb} = k_{gb} D^{-\frac{1}{2}} \tag{36}$$

where k_{gb} is a constant. For the solid-solution strengthening, when solute atoms dissolved into the matrix, distortion of the matrix lattice occurred, increasing the migration resistance of dislocations and contributing to the increasing strength. The degree of strengthening was affected by the size difference, valence electrons, and moduli between the matrix and the solute atoms. The increase in critical shear stress of decomposition caused by the solid-solution elements can be expressed as:

$$\tau_{ss} = \sum A_i c_{ss,i}^{\frac{2}{3}} \tag{37}$$

where A_i is a constant. The precipitation strengthening was calculated by the Orowan strengthening theory. Among the many equations based on the Orowan theory, the most common one is the Orowan-Ashby equation (Ref. 37):

$$\tau_{prec} = \frac{0.13Gb}{\lambda} ln \frac{r}{b} \tag{38}$$

where G is the shear modulus of aluminum and λ is the mean distance of precipitations that can be calculated from volume fraction and radius of the precipitations. The dislocation strengthening can be calculated as follows (Ref. 38):

$$\tau_{dis} = \alpha Gb\sqrt{\rho} \tag{39}$$

where α is a constant.

Tensile model. To determine the global mechanical properties of the joint, a CSM simulation was conducted to obtain the structural response of the virtual joint via the Abaqus software. The local strength was calculated above, and the elongation was converted according to the ratio of the local strength to the strength of the base metal (BM). In Part 2

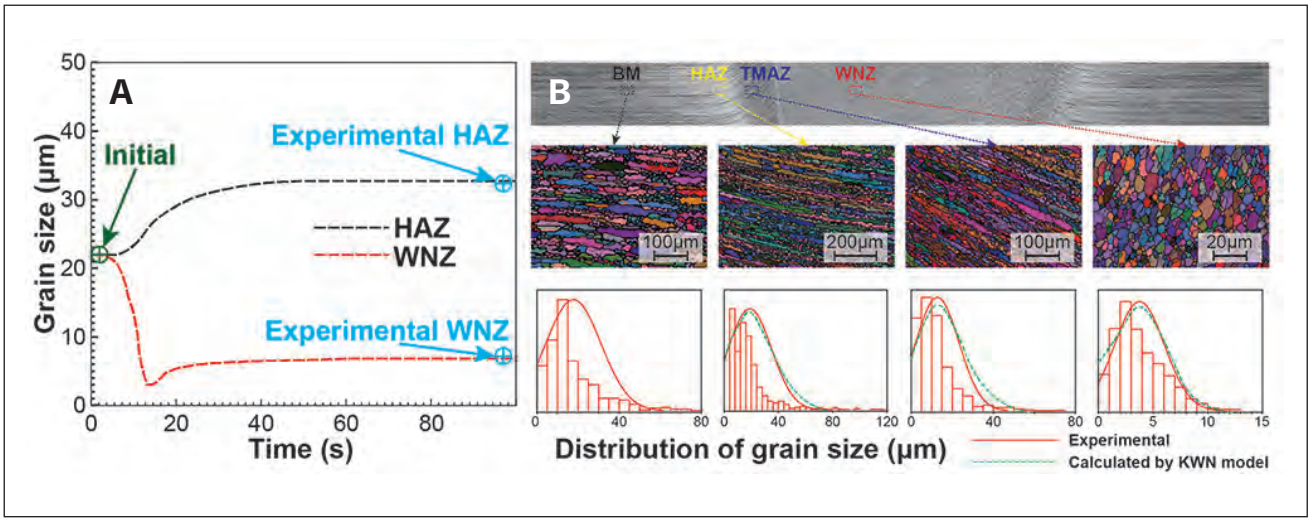

Fig. 8 — Variations of grain sizes during FSW: A — Average diameter calculated by GDRX model of the HAZ and WNZ with the stationary shoulder; B — inverse pole figures and distribution of grain sizes in welding joints via EBSD.

of this research (Ref. 18), the output value (global tensile strength) will be used for the final output of the subsequent neural network.

Results and Discussion

Calculated Causative Variables and Experimental Validations

Figure 3 shows the friction stir welded specimens' surficial and macro morphologies achieved with typical welding parameters. The value of welding thinning was directly related to the tilt angle and plunge depth. Excessive welding thinning will contribute to a severe drop in load-bearing capacity at the WNZ (Ref. 39). The issue of weld thinning was also seen in the subsequent CSM tensile model. The macrostructures reflected the formation characteristics of the joint with different combinations of welding parameters, including rotational or stationary shoulder, welding speed, and rotational velocity. The stationary shoulder, greater welding speed, and lower rotational velocity contributed to a lower heat input, which is usually a necessary and sufficient condition for better joint performances under the premise of no welding defects. However, these parameters are highly coupled. It is difficult to isolate and analyze every single parameter without being dependent on pure experimental methods. Therefore, the CFD method was applied to access the static and dynamic distributions of temperature and flow behaviors in the welding process.

The calculated field data via CFD methods are shown in Fig. 4. The temperature around the welding tool was significantly high. The highest temperature was located at the rear side of the shoulder, which was caused by the plunge depth due to the tilt angle. This angle concentrated more axial pressure in the rear side of the welding tool, thereby increasing frictional heat. The temperature of the advancing side was higher than that of the retreating side. The overall distribution of the temperature field showed an ellipsoidal shape (Ref. 25). This unique temperature distribution affected the macro- and microstructural evolution of the joint. Materials at high temperatures tend to quickly migrate the grain boundaries, and they have high diffusion rates, resulting in significant DRX and precipitation evolution.

Additionally, the thermoplasticized materials brought on by high temperature play a critical role in joint formation. Sufficient heat input guarantees the fluidity of the materials, thus obtaining defect-free joints. Figure 4C shows the comparison between the calculated and experimental data. The peak temperature relative error of less than 2% shows that the proposed CFD model was reasonable and accurate. For the rotating and nonrotating shoulders, the shape of the WNZ on the cross section was almost consistent with the simulated results — Fig. 6D, E. These results proved that the CFD model and its field output could be reliably applied to subsequent microstructural models and neural networks in Part 2 of this research (Ref. 18).

Although the thermal cycle is one of the major prerequisites for sound joints, the joining of BMs was not only obtained by thermal diffusion. Severe plastic deformation was another characteristic. The global and local material flow driven by the welding tool contributed to the main formation behaviors, including metallurgical reactions and mechanical interlocking. The material flow around the welding tool can be expressed via strain rate, a quantitative scalar of the velocity gradient tensor. A higher strain rate resulted in several aspects: (a) a more uniform and more frequent blending of the thermoplasticized materials occurred, improving the load-bearing capacity of the joints; (b) a higher velocity gradient brought on spatial discontinuity in the material flow, which potentially promoted the initiation of welding defects; and (c) more heat input was introduced by the greater strain rate in the form of deformation heat.

However, heat input tends to be reduced in most FSW processes. Higher heat input coarsens grains and precipitations,

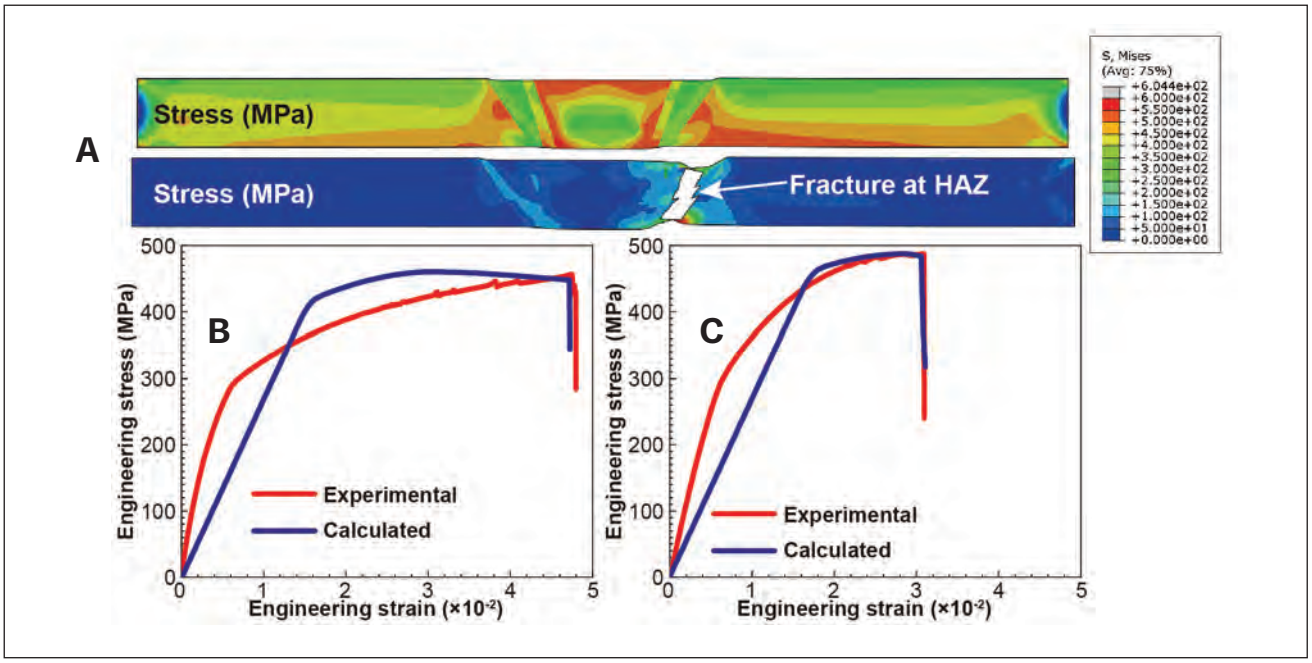

Fig. 9 — Results of the CSM tensile simulation: Typical results (A) comparison of calculated curves and tensile tests with the rotating shoulder (B) and the stationary shoulder (C).

which deteriorates the mechanical properties of the joints. The strain rate of the thermoplasticized AA2195 alloy was affected by the transient distributions of velocities around the welding tool. Figure 4B shows the contour of the strain rate around the welding tool. The strain rate decreased rapidly with increasing distance from the welding tool, which was consistent with the observations in other peer-reviewed literature (Ref. 40). In addition, the local strain rate significantly affected the pin morphologies. The milling facets and threads increased the strain rate, thereby improving the joint formation and increasing the tendency for welding defects.

The above discussion is based on the observation of the contour. However, quantitative data were necessary to directly make the outputs applicable for the subsequent neural networks in Part 2 of this research (Ref. 18) to read such a highly nonlinearly coupled field dataset. Figure 5A and B depict the evolution of the temperature and strain rate along the streamlines of different models. These curves represent the thermal cycle and plastic deformation experienced by each cell throughout the welding process. With these changes in strain rate and temperature, speculations can be made on microstructural behaviors, including DRX and precipitation evolutions. In addition, the curves extracted from the pin with complex structures brought on a greater velocity gradient — Fig. 5C, D. The stationary shoulder was also capable of reducing the heat input. This proved that the extracted data was reliable.

It is worth noting that ameliorating the joint formation by increasing the strain rate was a double-edged sword, which has been mentioned above several times (Ref. 41). The initiation possibility of welding defects increased with the appearance of complex structures located on the welding tools. This possibility was difficult to evaluate with a simple CFD model. Lower heat input was equivalent to the better load-bearing capacity of welding joints if welding defects were ignored. This is unacceptable for a systematic calculation model.

Therefore, a defect prediction model based on the discrete phase model was utilized to characterize the forming characteristics of the joint formation. Figure 6 shows the distribution of massless particles generated by a discrete phase model with different welding parameters. Compared with Fig. 3, the crimson area in the WNZ corresponds to the welding defects. The formation index correlates well with the experimental distribution of welding defects. The performance of the joint with defects dropped sharply, which happens when the heat input is too low and the strain rate is not sufficient. This index was applied to predict the global tensile strength of the joint, thus avoiding the appearance of unacceptable results. By combining the CFD and discrete phase models, a model that can effectively predict macrostructural evolution during welding was successfully implemented.

Microstructural Evolutions

Because the weight fractions of Cu and Li were about 4% and 1%, no δ' phase existed. Instead, large amounts of T_1 and θ''/θ' phases existed (Ref. 26). However, these experimental results obtained by high-resolution transmission electron microscopy can only obtain the distributions of precipitations before and after welding. The microstructural evolution during the welding process cannot be monitored by experimental means. The modified KWN model provides a preferred solution.

As shown in Fig. 7, the evolution of precipitations in the WNZ of the rotating shoulder and stationary shoulder under their respective typical parameters exhibited different characteristics. Both firstly experienced a rapid heating process.

Precipitations, including T_1 and θ''/θ' phases, first underwent solid solution. Due to the rapid increase in temperature, the size of most of the strengthening phases was smaller than their critical radius, according to Equation 24. The average diameter and volume fraction decreased sharply. The Cu and Li elements in the matrix entered the supersaturated solid-solution state. Additionally, high-density dislocations and DRXed grain boundaries were generated due to the severe plastic deformation during FSW. These sites provided the necessary conditions for the nucleation of new precipitations in the subsequent cooling process (Ref. 30). These promoted the generation of the uniform and fine T_1 and θ''/θ' phases.

Decreus et al. (Ref. 26) pointed out that the evolution kinetics of these two strengthening phases were significantly affected by plastic deformation. Their distributions depended on the local concentration of the Li element. The T_1 phase preferentially nucleated in the area with high-density dislocations induced by the FSW process and gradually approached the saturation state. Then, due to the local depletion of the Li element, the θ''/θ' phase appeared in the area where the T_1 phase had not yet been formed. This explains why the formation of the T_1 phase was relatively earlier than the θ''/θ' phase, which proves the rationality of the calculates curve.

In addition, in the case of the rotating shoulder, the precipitations entirely dissolved due to the higher heat input in the heating process. The higher temperature also brought on a greater critical nucleation radius, making the initial size of precipitation larger and the nucleation rate lower. However, the volume fraction of the joint was still high. The coarser precipitations reduced their strengthening effect (Ref. 34). Furthermore, due to massive precipitations, the proportion of solid-solution strengthening also decreased, although solid-solution strengthening was not the key strengthening mechanism for the Al-Cu-Li alloys. By contrast, in the case of the stationary shoulder, the great reduction in heat input caused the peak temperature to drop by about 20%. The precipitations only partially dissolved during the heating process. In the subsequent cooling process, the lower temperature contributed to a smaller critical nucleation radius, which effectively improved the precipitation strengthening effect.

The transformation of precipitations is the embodiment of the precipitation strengthening effect. However, the load-bearing capacity of the heat-treated strengthening aluminum alloy does not depend solely on this. The Hall-Petch effect and dislocation strengthening are also not negligible (Ref. 17). Figure 8 shows the calculated and experimental results of DRX at the WNZ and HAZ based on the geometric DRX model. Due to severe plastic deformation, the materials in the WNZ quickly underwent DRX with sufficient strain rates and transformed from a deformed microstructure to fine equiaxed crystal microstructures. We have assumed that the materials did not undergo the second DRX. These materials in the nugget gradually recovered under the co-effects of subsequent heat and plastic deformation, resulting in a gradual increase in grain size. One can see from Equation 34 that the enhancement of strain rate can effectively suppress the coarsening of the grains, while the increases in temperature will accelerate the growth of grains. Therefore, our goal is to achieve a combination of low peak temperature and high strain rate without welding defects. In addition, the HAZ is also a major component, which usually manifests as the weakness of the joints. There is no strain rate and accumulated plastic strain, so DRX does not occur in the HAZ. Throughout the calculation process, only the static recovery was observed, leading to the gradual increase of the grain sizes while the dislocation density gradually decreased. This has a negative impact on both fine-grain strengthening and dislocation strengthening. Thus, FSW joints usually break at or near the HAZ during the unidirectional tensile test.

The strengthening effects on the local area were obtained using the aforementioned analyses. The local strength of any location on the joints could be calculated. These values considered various strengthening mechanisms and weakening effects of welding defects. However, the actual tensile strength of the whole joint was the reflection of all the cells in the welding joints. Applying these local values to a two-dimensional CSM tensile model was a good choice. The local elongation was generated by referring to the local strength in a linear ratio. Figure 9 shows the dynamic stress distribution and fracture position. This result was obtained from the typical parameters of the stationary shoulder. The stress-strain curves were obtained by calculating the stress evolution on the CSM model — Fig. 9B, C. It matched the experimental curves well, which shows that the aforementioned micro-evolution model is reasonable. As such, the macro- and microstructural responses of the friction stir welded joints, which provided datasets for the following neural network in Part 2 of this research (Ref. 18), were successfully integrated.

Conclusions

An entire process-simulation strategy was proposed to map the macro- and microstructural responses of friction stir welded aluminum alloys. Owing to their more-complex phase composition and precipitations, AA2195-T8 alloys were chosen as the research object. This model adopted a series of numerical models, including the CFD model, modified KWN model, DRX and recovery model, and CSM model. The comparison between experimental results and the combined model proved the rationality and accuracy of this numerical model. This combined model will provide the necessary datasets for the following neural network methods in Part 2 of this research (Ref. 18).

Acknowledgments

This work was jointly supported by the National Natural Science Foundation of China (No. 52175301) and the Heilongjiang Postdoctoral Foundation (No. LBH-Z20055).

Appendix I: Physical and Empirical Parameters

All the physical and empirical parameters used in the numerical models in this paper are listed in Table A1.

Table A1 — Physical and Empirical Parameters Used in Numerical Models

Parameter	Symbol	Value
Material constant #1 of AA2195-T8	α	1.1×10^{-8} Pa^{-1}
Material constant #2 of AA2195-T8	A	3.77×10^{8}
Material constant #3 of AA2195-T8	n	3.55
Influencing factor of AA2195-T8	γ	0.4
Activation energy of Sellars-Tegart constitutive equation of AA2195-T8	Q_{zh}	1.52×10^{5} J/mol
Gas constant	R	8.314 J/(mol·K)
Solidus temperature of AA2195-T8	T_s	807 K
Empirical coefficient #1	β_1	0.8
Empirical coefficient #2	β_2	0.7
Friction coefficient	μ	0.4
Axial pressure	P	65 MPa
Interfacial constant	δ_0	0.4
Thermal conductivity of AA2195-T8	$k_D(T)$	92.5 + 0.17*T W/(m·K)
Thermal conductivity of H13	k_T	29 W/(m·K)
Thermal conductivity of M42	k_T	20 W/(m·K)
Thermal conductivity of WC-Co	k_T	85 W/(m·K)
Thermal conductivity of W-Re	k_T	21 W/(m·K)
Thermal conductivity of polycrystalline cubic boron nitride (PCBN)	k_T	79 W/(m·K)
Density of AA2195-T8	ρ_D	2690 kg/m^3
Density of steel	ρ_T	7800 kg/m^3
Density of WC-Co	ρ_T	15630 kg/m^3
Density of W-Re	ρ_T	19650 kg/m^3

Table A1 — (continued)

Parameter	Symbol	Value
Density of PCBN	ρ_T	2250 kg/m^3
Heat capacity of AA2195-T8	$C_{pD}(T)$	703 + 0.373*T + 0.00155*T^2 J/(kg·K)
Heat capacity of H13	C_{pT}	470 J/(kg·K)
Heat capacity of M42	C_{pT}	450 J/(kg·K)
Heat capacity of WC-Co	C_{pT}	280 J/(kg·K)
Heat capacity of W-Re	C_{pT}	120 J/(kg·K)
Heat capacity of PCBN	C_{pT}	970 J/(kg·K)
Heat transfer coefficient of upper and side wall	h_w	15 W/(m^2·K)
Heat transfer coefficient of lower wall	h_{lw}	130 W/(m^2·K)
Stefan-Boltzmann constant	σ	5.67×10^{-8} W/(m^2·K^4)
Emissivity of AA2195-T8	ε	0.35
Diffusion factor of Cu element	$D_{O,Cu}$	6.5×10^{-5} m^2/s
Diffusion factor of Li element	$D_{O,Li}$	4.7×10^{-5} m^2/s
Diffusion activation energy of Cu element	$Q_{d,Cu}$	1.35×10^5 J/mol
Diffusion activation energy of Li element	$Q_{d,Li}$	1.03×10^5 J/mol
Interfacial energy of T_1	$\gamma_{int,T1}$	0.23 J/m^2
Interfacial energy of θ variants	$\gamma_{int,\theta}$	0.2 J/m^2
Molar volume of T_1	$V_{m,T1}$	3.15×10^{-5} m^3/mol
Molar volume of θ variants	$V_{m,\theta}$	2.85×10^{-5} m^3/mol
Concentration constant of T_1	$C_{eO,T1}$	10.35
Concentration constant of θ variants	$C_{eO,\theta}$	9.68
Dissolution enthalpy of T_1	$Q_{e,T1}$	4.87×10^4 J/mol
Dissolution enthalpy of θ variants	$Q_{e,\theta}$	4.62×10^4 J/mol
Nucleation constant #1 of T_1	$J_{0,T1}$	1.035×10^{35}/(m^3·s)
Nucleation constant #1 of θ variants	$J_{0,\theta}$	9.67×10^{34}/(m^3·s)

Table A1 — (continued)

Parameter	Symbol	Value
Nucleation constant #2 of T_1	$A_{O,T1}$	1.92×10^4 J/mol
Nucleation constant #2 of θ variants	$A_{O,\theta}$	1.63×10^4 J/mol
Geometric constant	K_s	11.0
DRX constant #1	a	-3.43×10^{-9} m^{-1}
DRX constant #2	b	0.16×10^{-9} m^{-1}
Migration coefficient	M_0	$5 \times 10^{-6} \times m^2/s$
Grain boundary energy	γ_b	0.3 J/m^2
Migration activation energy	Q_G	7.7×10^4 J/mol
Sensitivity coefficient of defects	X^p	3.0
Intrinsic strength of aluminum alloys	σ_{in}	16 MPa
Taylor factor	M	3.06
Hall-Petch constant	k_{gb}	0.065 MPa·$s^{1/2}$
Solid-solution strengthening constant of Cu	A_{Cu}	12.431
Solid-solution strengthening constant of Li	A_{Li}	23.772
Shear modulus	G	26 GPa
Burgers vector	b	2.84×10^{-10} m
Dislocation strengthening constant	a	0.3

References

1. Meng, X., Huang, Y., Cao, J., Shen, J., and dos Santos, J. F. 2021. Recent progress on control strategies for inherent issues in friction stir welding. *Progress in Materials Science* 115: 100706. DOI: 10.1016/j.pmatsci.2020.100706

2. Mishra, R. S., and Ma, Z. Y. 2005. Friction stir welding and processing. *Materials Science and Engineering: R: Reports* 50(1–2): 1–78. DOI: 10.1016/j.mser.2005.07.001

3. Xie, Y., Meng, X. , Li, Y. , Mao, D. , Wan, L. , and Huang, Y. 2021. Insight into ultra-refined grains of aluminum matrix composites via deformation-driven metallurgy. *Composites Communications* 26: 100776. DOI: 10.1016/j.coco.2021.100776

4. Xie, Y., Meng, X., Mao, D., Chang, Y., Qin, Z., Ma, X., Wan, L., and Huang, Y. 2022. Deformation-driven modification of Al-Li-Mg-Zn-Cu high-alloy aluminum as anodes for primary aluminum-air batteries. *Scripta Materialia* 212: 114551. DOI: 10.1016/j.scriptamat.2022.114551

5. Sun, Z., and Wu, C. S. 2018. A numerical model of pin thread effect on material flow and heat generation in shear layer during friction stir welding. *Journal of Manufacturing Processes* 36: 10–21. DOI: 10.1016/j.jmapro.2018.09.021

6. Tongne, A., Desrayaud, C., Jahazi, M., and Feulvarch, E. 2017. On material flow in friction stir welded Al alloys. *Journal of Materials Processing Technology* 239: 284–296. DOI: 10.1016/j.jmatprotec.2016.08.030

7. Wang, T., Ramírez-Tamayo, D., Jiang, X., Kitsopoulos, P., Kuang, W., Gupta, V., Barker, E., and Upadhyay, P. 2020. Effect of interfacial characteristics on magnesium to steel joint obtained using FAST. *Materials & Design* 192: 108697. DOI: 10.1016/j.matdes.2020.108697

8. Ji, S., Li, Z., Wang, Y., and Ma, L. 2017. Joint formation and mechanical properties of back heating assisted friction stir welded Ti–6Al–4V alloy. *Materials & Design* 113: 37–46. DOI: 10.1016/j.matdes.2016.10.012

9. Simar, A., Bréchet, Y., de Meester, B., Denquin, A., Gallais, C., and Pardoen, T. 2012. Integrated modeling of friction stir welding of 6xxx series Al alloys: Process, microstructure and properties. *Progress in Materials Science* 57(1): 95–183. DOI: 10.1016/j.pmatsci.2011.05.003

10. Huang, Y., Xie, Y., Meng, X., Lv, Z., and Cao, J. 2018. Numerical design of high depth-to-width ratio friction stir welding. *Journal of Materials Processing Technology* 252: 233–241. DOI: 10.1016/j.jmatprotec.2017.09.029

11. Ji, S. D., Wen, Q., and Li, Z. W. 2020. A novel friction stir diffusion bonding process using convex-vortex pin tools. *Journal of Materials Science & Technology* 48: 23–30. DOI: 10.1016/j.jmst.2020.01.042

12. Su, H., Wu, C. S., Pittner, A., and Rethmeier, M. 2014. Thermal energy generation and distribution in friction stir welding of aluminum alloys. *Energy* 77: 720–731. DOI: 10.1016/j.energy.2014.09.045

13. Arora, A., De, A., and DebRoy, T. 2011. Toward optimum friction stir welding tool shoulder diameter. *Scripta Materialia* 64(1): 9–12. DOI: 10.1016/j.scriptamat.2010.08.052

14. Wu, L. H., Hu, X. B., Zhang, X. X., Li, Y. Z., Ma, Z. Y., Ma, X. L., and Xiao, B. L. 2019. Fabrication of high-quality Ti joint with ultrafine grains using submerged friction stirring technology and its microstructural evolution mechanism. *Acta Materialia* 166: 371–385. DOI: 10.1016/j.actamat.2018.12.059

15. dos Santos, J. F., Staron, P., Fischer, T., Robson, J. D., et al. 2018. Understanding precipitate evolution during friction stir welding of Al-Zn-Mg-Cu alloy through in-situ measurement coupled with simulation. *Acta Materialia* 148: 163–172. DOI: 10.1016/j.actamat.2018.01.020

16. Irani, M., Lim, S., and Joun, M. 2019. Experimental and numerical study on the temperature sensitivity of the dynamic recrystallization activation energy and strain rate exponent in the JMAK model. *Journal of Materials Research and Technology* 8(2): 1616–1627. DOI: 10.1016/j.jmrt.2018.11.007

17. Xie, Y., Huang, Y. , Wang, F., Meng, X., Li, J., Dong, Z., and Cao, J. 2020. Deformation-driven metallurgy of SiC nanoparticle reinforced aluminum matrix nanocomposites. *Journal of Alloys and Compounds* 823: 153741. DOI: 10.1016/j.jallcom.2020.153741

18. Xie, Y., Meng, X., and Huang, Y. 2022. Entire-process simulation of friction stir welding — Part 2: Implementation of neural networks. *Welding Journal* 101(6). Forthcoming.

19. Huang, Y., Wan, L., Meng, X., Xie, Y., Lv, Z., and Zhou, L. 2018. Probe shape design for eliminating the defects of friction stir lap welded dissimilar materials. J*ournal of Manufacturing Processes* 35: 420–427. DOI: 10.1016/j.jmapro.2018.08.026

20. Pei, X., and Dong, P. 2017. A selectively-coupled shear localization model for friction stir welding process window estimation. *International Journal of Machine Tools and Manufacture* 123: 89–104. DOI: 10.1016/j.ijmachtools.2017.08.003

21. Cho, H. H., Hong, S. T., Roh, J. H., Choi, H. S., Kang, S. H., Steel, R. J., and Han, H. N. 2013. Three-dimensional numerical and experimental investigation on friction stir welding processes of ferritic stainless steel. *Acta Materialia* 61(7): 2649–2661. DOI: 10.1016/j.actamat.2013.01.045.

22. Zienkiewicz, O. C., and Cormeau, I. C. 1974. Visco-plasticity — Plasticity and creep in elastic solids — A unified numerical solution approach. *International Journal for Numerical Methods in Engineering* 8(4): 821–845. DOI: 10.1002/nme.1620080411

23. Zhao, W., and Wu, C. 2019. Constitutive equation including acoustic stress work and plastic strain for modeling ultrasonic vibration assisted friction stir welding process. *International Journal of Machine Tools and Manufacture* 145: 103434. DOI: 10.1016/j.ijmachtools.2019.103434

24. Mendez, P. F., Tello, K. E., and Lienert, T. J. 2010. Scaling of coupled heat transfer and plastic deformation around the pin in friction stir welding. *Acta Materialia* 58(18): 6012–6026. DOI: 10.1016/j.actamat.2010.07.019

25. He, X., Gu, F., and Ball, A. 2014. A review of numerical analysis of friction stir welding. *Progress in Materials Science* 65: 1–66. DOI: 10.1016/j.pmatsci.2014.03.003

26. Decreus, B., Deschamps, A., De Geuser, F., Donnadieu, P., Sigli, C., and Weyland, M. 2013. The influence of Cu/Li ratio on precipitation in Al–Cu–Li–x alloys. *Acta Materialia* 61(6): 2207–2218. DOI: 10.1016/j.actamat.2012.12.041

27. Deschamps, A., and Brechet, Y. 1998. Influence of predeformation and ageing of an Al–Zn–Mg alloy — II. Modeling of precipitation kinetics and yield stress. *Acta Materialia* 47(1): 293–305. DOI: 10.1016/S1359-6454(98)00296-1

28. Han, J., Thomas, S. L., and Srolovitz, D. J. 2018. Grain-boundary kinetics: A unified approach. *Progress in Materials Science* 98: 386–476. DOI: 10.48550/arXiv.1803.03214

29. Ruoff, A. L., and Balluffi, R. W. 1963. Strain-enhanced diffusion in metals. II. Dislocation and grain-boundary short-circuiting models. *Journal of Applied Physics* 34(7): 1848–1853. DOI: 10.1063/1.1729698

30. Xie, Y., Meng, X., Wang, F., Jiang, Y., Ma, X., Wan, L., and Huang, Y. 2021. Insight on corrosion behavior of friction stir welded AA2219/AA2195 joints in astronautical engineering. *Corrosion Science* 192: 109800. DOI: 10.1016/j.corsci.2021.109800

31. Du, Q., Tang, K., Marioara, C. D., Andersen, S. J., Holmedal, B., and Holmestad, R. 2017. Modeling over-ageing in Al-Mg-Si alloys by a multi-phase CALPHAD-coupled Kampmann-Wagner numerical model. *Acta Materialia* 122: 178–186. DOI: 10.1016/j.actamat.2016.09.052

32. Ma, Z. Y., Feng, A. H., Chen, D. L., and Shen, J. 2018. Recent advances in friction stir welding/processing of aluminum alloys: Microstructural evolution and mechanical properties. *Critical Reviews in Solid State and Materials Sciences* 43(4): 269–333. DOI: 10.1080/10408436.2017.1358145

33. Speight, M. V. 1968. Growth kinetics of grain-boundary precipitates. *Acta Metallurgica* 16(1): 133–135. DOI: 10.1016/0001-6160(68)90081-3

34. Xie, Y., Meng, X., Chang, Y., Mao, D., Yang, Y., Xu, Y., Wan, L., and Huang, Y. 2022. Ameliorating strength-ductility efficiency of graphene nanoplatelet-reinforced aluminum composites via deformation-driven metallurgy. *Composites Science and Technology* 219: 109225. DOI: 10.1016/j.compscitech.2021.109225

35. Hu, P., Liu, Y., Zhu, Y., and Ying, L. 2016. Crystal plasticity extended models based on thermal mechanism and damage functions: Application to multiscale modeling of aluminum alloy tensile behavior. *International Journal of Plasticity* 86: 1–25. DOI: 10.1016/j.ijplas.2016.07.001

36. Hansen, N. 2004. Hall–Petch relation and boundary strengthening. *Scripta Materialia* 51(8): 801–806. DOI: 10.1016/j.scriptamat.2004.06.002

37. Chen, B., Shen, J. , Ye, X., Jia, L., Li, S., Umeda, J., Takahashi, M., and Kondoh, K. 2017. Length effect of carbon nanotubes on the strengthening mechanisms in metal matrix composites. *Acta Materialia* 140: 317–325. DOI: 10.1016/j.actamat.2017.08.048

38. Huskins, E. L., Cao, B., and Ramesh, K. T. 2010. Strengthening mechanisms in an Al–Mg alloy. *Materials Science and Engineering: A* 527(6): 1292–1298. DOI: 10.1016/j.msea.2009.11.056

39. Guan, M., Wang, Y., Huang, Y., Liu, X., Meng, X., Xie, Y., and Li, J. 2019. Non-weld-thinning friction stir welding. *Materials Letters* 255: 126506. DOI: 10.1016/j.matlet.2019.126506

40. Feulvarch, E., Roux, J. C., and Bergheau, J. M. 2013. A simple and robust moving mesh technique for the finite element simulation of friction stir welding. *Journal of Computational and Applied Mathematics* 246: 269–277. DOI: 10.1016/j.cam.2012.07.013

41. Huang, Y., Xie, Y., Meng, X., Li, J., and Zhou, L. 2019. Joint formation mechanism of high depth-to-width ratio friction stir welding. *Journal of Materials Science & Technology* 35(7): 1261–1269. DOI: 10.1016/j.jmst.2019.01.016

YUMING XIE, **XIANGCHEN MENG**, and **YONGXIAN HUANG** (*yxhuang@hit.edu.cn*) are with the State Key Laboratory of Advanced Welding and Joining, Harbin Institute of Technology, Harbin, China.